Preliminary results and structural interpretations from drone lidar surveys over the Eastern Denali fault, Yukon

Theron Finley*, Guy Salomon and Edwin Nissen
School of Earth and Ocean Sciences, University of Victoria

Roger Stephen
Department of Geography, University of Victoria

John Cassidy
Pacific Geoscience Centre, Geological Survey of Canada, Natural Resources Canada

Brian Menounos
Department of Geography, Earth, and Environmental Sciences, University of Northern British Columbia

Finley, T., Salomon, G., Stephen, R., Nissen, E., Cassidy, J. and Menounos, B., 2022. Preliminary results and structural interpretations from drone lidar surveys over the Eastern Denali fault, Yukon. *In:* Yukon Exploration and Geology 2021, K.E. MacFarlane (ed.), Yukon Geological Survey, p. 83–105.

Abstract

The Yukon Geological Survey and Kluane First Nation intend to drill a temperature gradient well near Burwash Landing, YT, to evaluate the geothermal energy potential of the area. The preferred drill site is located immediately southwest of the Eastern Denali fault (EDF), which has ruptured multiple times in the Holocene. The kinematics and recent activity of the fault are important factors to consider when developing a geothermal resource, for two purposes: 1. identifying zones of enhanced permeability due to local fault geometry and 2. assessing the seismic hazard of drilling and developing a geothermal system along an active fault. Here, we present new lidar data collected from a drone platform, which enabled the production of 30 cm spatial resolution bare-earth Digital Terrain Models (DTMs) over several segments of the EDF. These products offer a considerable increase in both spatial resolution and canopy penetration compared to existing spaceborne and airborne photogrammetric Digital Surface Models (DSMs) and DTMs of the area. We use hillshades to map segments of the EDF surface trace in detail, and we make preliminary interpretations about the structure and kinematics of the fault. Offset stream channels and hill slopes that cross the fault at high angles indicate dextral offsets ranging between 5 and 75 m. Vertical separation ranges between 0 and 20 m, varying between northeast and southwest-side up. We confirm previous interpretations that the geothermal drill site is located at a minor releasing bend in the fault. Previous fault maps based on ArcticDEM data showed multiple fault splays parallel to the EDF at the geothermal drill site, whereas the lidar data indicate strain is concentrated to a singular fault plane in this area. The EDF is characterized by a series of sediment mounds that we interpret to be positive flower structures. The higher spatial resolution achieved by the drone reveals possible compressional structures (fault tips or folds) consistent with dextral transpression on the surface of these mounds. We recommend additional drone lidar acquisition, field studies, geophysical analysis, and kinematic modeling to be carried out over the coming year.

* tfinley@uvic.ca

Introduction & Motivation

Geothermal Resource Exploration

As part of an effort to assess the potential for geothermal resource extraction in Yukon, the Yukon Geological Survey (YGS) is working with the Kluane First Nation (KFN) to drill a temperature gradient well near the community of Burwash Landing, YT. Burwash Landing is a small community of <100 people and is one of several remote communities in the territory that still relies on diesel fuel for electricity generation. Geothermal energy could, at the very least, provide direct heating for buildings, offsetting demand for electricity. There is particular interest in using geothermal energy for greenhouses, thereby contributing to food security in the community. If the geothermal resource is hot enough, it could also be used for electricity generation. Geothermal energy is one of only a few renewable energy sources that provides base-load (non-intermittent) power, and it does so while emitting very little carbon and requiring minimal physical infrastructure (Kristmannsdóttir and Ármannsson, 2003; IPCC, 2014). Discovering a geothermal resource would be highly beneficial for this community, and Yukon as a whole.

Geothermal conditions in Yukon are generally favourable for development; terrestrial heat flow is in the range of 80–100 mW m^{-2} over a broad area of the territory, which is comparable to values in geothermal fields in the southwestern United States (Blackwell and Richards, 2004; Majorowicz and Grasby, 2010). Despite the high heat flow, there are limited expressions of geothermal activity at the surface (e.g., thermal springs). If significant geothermal resources do exist, they are mostly "blind", suppressed from reaching the surface by permeable surficial deposits, or shallow, cold groundwater plumes (Dobson, 2016). To de-risk drilling, predictive mapping using a variety of geological and geophysical techniques must be employed to prioritize the most favourable zones. Geothermal resources in Yukon are likely amagmatic, fault-controlled, convective hydrothermal systems (Moeck, 2014). In this resource type—best exemplified by the geothermal systems in the Basin and Range province of Nevada—major fault zones act both as reservoirs and conduits for fluid, facilitating deep circulation into the crust (Faulds and Hinz, 2015; Jolie *et al.*, 2015; Craig, 2018). As has been demonstrated in the Basin and Range, detailed mapping of structural features and neotectonic setting can facilitate prediction of where plumes of thermal water might reach economic drilling depths (Faulds *et al.*, 2016; Craig, 2018).

The fault zone that is of interest for geothermal exploration near Burwash Landing is the Eastern Denali fault (EDF), a major Holocene-active structure with significant strike-slip, and possibly dip-slip offset. It has been speculated that the EDF might provide the necessary permeability to allow thermal fluid to ascend to the near surface where it might be economically accessible via drilling (Witter, 2020). A critical part of the geothermal exploration process in fault-controlled domains is locating specific segments of the fault that are likely to be most permeable, and host to the greatest volume of thermal fluid. There are several related factors that contribute to fault permeability, the most important of which are: fault age, strain rate, stress orientation and kinematics. Young, seismically active faults are generally more permeable due to episodic refracturing of mineral precipitate that would otherwise seal the fault (Curewitz and Karson, 1997). Faults with higher strain rate are also generally more permeable, because the re-fracturing occurs more frequently (Faulds *et al.*, 2012). Faults that are oriented favourably in the stress field for slip or dilation tend to remain more permeable, whereas those oriented perpendicular to the stress-field are clamped shut (Meixner *et al.*, 2016). Finally, fault kinematics play a role in the directionality of fluid flow; it has been shown that fluid tends to flow preferentially parallel to σ_2, which implies that strike-slip faults are more conducive to vertical convection of fluid (Sibson, 1996). In the well-studied structurally-controlled geothermal fields of Nevada and elsewhere, detailed structural mapping combined with geophysical data has allowed for the identification of the most favourable structural settings (Curewitz and Karson, 1997; Faulds and Hinz, 2015). These settings include fault tips, stepovers and relays, and intersections where increased fracture density favours hydrothermal upwelling.

There are several methods that are useful for constraining the parameters most relevant to geothermal fluid flow: field-based structural geology, remote sensing, geodesy, and seismology. In a pilot study of geothermal resource potential along the Tintina Fault near Ross River, field-based structural mapping was used to constrain crustal strain, and thus target specific fault strands identified in geophysical models and bedrock mapping (Mira Geoscience, 2015). However, mapping of strain preserved in geologic structures does not reliably provide information about current stress and strain, only strain that occurred sometime in the past. Remote sensing (e.g., LiDAR), geodesy and seismology are therefore helpful tools to evaluate the current tectonic setting of fault-controlled geothermal resources. In a comprehensive early assessment of the geothermal system at Burwash Landing, Witter (2020) used existing photogrammetric DSMs and DTMs (Bender and Haeussler, 2017; Porter *et al.*, 2018) to map out the surface trace of the Denali fault. However, these existing data sets are not quite adequate for the purposes of Holocene fault mapping as they are not true bare-earth DTMs with vegetation stripped away. A key recommendation put forth by Witter (2020) was the acquisition of lidar over the project area to accurately map Holocene faults, and distinguish faults from glacial lineations that run parallel to the EDF. This recommendation was echoed by Blais-Stevens *et al.* (2020) as a means to better understand the kinematics and seismic history of the fault. This report details our efforts to begin to address this data gap.

Previous paleoseismic and remote sensing studies of the EDF

In Alaska, the Central Denali fault has hosted large earthquakes in recorded history, including a M7.9 event in 2002 (Eberhart-Phillips *et al.*, 2003), but the seismic history and hazard on the EDF in Yukon are less well constrained despite nearly 70 years of study. Some of the earliest maps of the EDF were produced by Bostock (1952) using air photos and extensive field investigations. It was possible to recognize the surface trace of the EDF at a broad level without sophisticated remote sensing techniques due to the preferential growth of Black Spruce on a series of sediment mounds that occur along the fault. Bostock recognized that the fault must be young due to the lack of glacial overprint on the fault scarp but did not specify an age range for past ruptures. Clague (1979) built on Bostock's work with further investigation of air photos and glacial geology. He was able to determine that the EDF had likely ruptured in the early and mid-Holocene, but not more recently than 500 years ago, based on undisturbed paleo-shorelines of Kluane Lake. Three paleoseismic trenches were excavated on the EDF near the Duke River by USGS, YGS and Simon Fraser University researchers (Seitz *et al.*, 2008; Lipovsky *et al.*, 2009) but the results were not formally published beyond conference abstracts. Blais-Stevens *et al.* (2020) re-excavated these trenches and integrated other data from lake sediment cores and exposures of Holocene sediment, ultimately concluding that up to four >M_w 6 events have occurred in the last 6000 years. Various geophysical studies have also examined the EDF: Leonard *et al.* (2008) used the earthquake catalog to estimate a slip rate of ~2 mm/yr across this segment of the fault and Marechal *et al.* (2015) obtained a similar slip rate from GNSS velocities. However, it has also been speculated that most of the strain accommodated on the Central Denali fault in Alaska is subsequently partitioned onto either a hypothetical "Connector Fault" through the St. Elias Mountains (Spotila and Berger, 2010; Marechal *et al.*, 2015) or in a diffuse zone to the southwest of the Eastern Denali fault (Choi *et al.*, 2021), in both cases bypassing the EDF itself.

Due to financial constraints, the EDF has not, until now, been widely covered by lidar data. Transport Canada has apparently previously flown lidar over the Denali fault, but these data have not been made available to researchers (Bender and Haeussler, 2017). Small sections of the Denali fault are also captured in lidar data acquired by Yukon Highways and Public Works (https://yukon.ca/en/statistics-and-data/mapping/view-yukon-elevation-data), but these are not sufficient for detailed mapping along strike. In an effort to complement lidar imagery acquired over the Alaskan segment of the Denali fault, Bender and Haeussler (2017) used Agisoft Photoscan (now Metashape) structure-from-motion software to create a 4 m-resolution DSM from legacy aerial photos. This DSM was then used to digitally

map the Denali fault. Marechal et *al.* (2018) also used aerial photogrammetry to measure geometry of distinct tectonic scarps along the fault, and the newly released ArcticDEM data set offers a 2 m-resolution DSM derived from satellite stereo-photographs. However, none of these data sets derived from optical imagery allow for the removal of vegetation from the landscape, adding uncertainty to locations and exact measurements of the fault scarp. In this report, we detail the acquisition of new high-resolution (30 cm pixel) bare earth lidar DTM from a drone platform.

Unanswered questions about the EDF

Despite the number of studies on the EDF, there remain several unanswered questions that lidar data may be able to help answer:

- Efforts to measure the vertical and lateral offset of the EDF have been challenged by large uncertainties in photogrammetric DSMs. For example, Haeussler et *al.* (2017) arrived at a rough estimate of 20–30 m dextral slip based on two offset groves of Black Spruce on sediment mounds. The total offset can be divided to estimate the magnitude of multiple individual events identified in previous studies (e.g., Blais-Stevens et *al.*, 2020). Additionally, lidar data may allow for the discernment of multiple rupture events from variations in marker offsets along strike (e.g., Zielke et *al.*, 2010).
- Limited structural mapping in the vicinity of the proposed geothermal drill site (Witter, 2020) has suggested that the EDF is a broad fault zone with multiple subparallel strands. Existing photogrammetric DSMs do not have the resolution to determine whether multiple strands have ruptured the surface sediments. Lidar data will help confirm whether these subtle parallel lineaments are fault-related or simply glacial features.
- The EDF is characterized by a series of sediment mounds that are interpreted to be positive flower structures (Haeussler et *al.*, 2017; Blais-Stevens et *al.*, 2020). The exact morphology of these mounds is imperfectly represented by the preferential growth of Black Spruce trees on them. Lidar data will allow for the removal of the trees to obtain more accurate measurement of their structure.
- Existing fault maps based on photogrammetric DSMs do not capture fine-scale (10–100 m) variations in fault strike. Lidar data will help identify and measure subtle releasing and restraining bends, which are of particular interest for identifying local zones of extension that may be more permeable to hydrothermal fluid flow.

Data and Methods

Drone Lidar

Over a 10-day period in September of 2021, high resolution lidar data were acquired using a Riegl miniVUX 1UAV lidar scanner mounted on a DJI M600 Pro drone platform (Fig. 1a); sensor position and orientation were concurrently logged with an Applanix APX-20 UAV GNSS-Inertial system. Flight mission and survey planning was done in Map Pilot Pro for iPadOS, utilizing a resampled 30 m resolution DSM derived from ArcticDEM as a baseline for terrain following. Individual flight lines were planned to provide a field of view of ± 30°, with 50% sidelap of adjacent flight lines. For each project area a set of orthogonal flight lines were acquired for boresight calibration. We used standardized flight parameters of 81 m above ground level at a speed of 6 m/s. One flight (Survey 3a) was conducted at half-speed (3 m/s) to acquire points at higher density over a subtle scarp feature. These chosen parameters reflect a trade off between areal coverage and point density that we have arrived at through experimentation. Lower and slower flights allow for data acquisition at much higher point densities, but the areal coverage possible in a single battery set is reduced. At the standard parameters, we achieved a point density of 35–40 pts/m^2 per flight line, and 70–80 pts/m^2 over the majority of each survey area where flight lines overlapped. Flight segments for an individual project area were limited in duration to approximately 20 minutes, necessitating multiple platform launches for most sites and continual recharging of battery sets throughout the day with an on-site generator. At typical survey acquisition parameters, we were able to cover an average of 0.25 km^2 for each set of batteries, although this coverage varied depending on the launch location, transit time to and from the survey, and weather conditions.

Transport Canada strictly regulates the operation of drones in Canada. All three field crew members possessed Advanced Small RPAS Pilot licenses. In every survey, the drone remained within visual line of sight (VLOS) of the pilot-in-command or a remote visual observer in contact via radio. The low height (10–20 m) and low density of the Black Spruce forests made the study area conducive to VLOS flight up to ~1.5 km from an observer. In addition to battery life, a major practical restriction on the length of each survey was connectivity with the controller, which degraded at ~1.5 km in some cases where there was obstructing terrain. In its current configuration, the entire drone system including GNSS survey equipment cannot be easily transported on foot, meaning that the drone must be launched from a site accessible by vehicle. This limitation prevented us from accessing remote segments of the EDF; in the future we hope to develop a more portable system.

A Trimble R12 Real-Time Kinematic Global Navigation Satellite System (RTK-GNSS) consisting of a static base station and a rover was deployed at each project area. The base station (Fig. 1a) was deployed in a location with a clear view of the sky for the length of the airborne survey, typically a few hours, logging GNSS observables. The logged base station data in RINEX format were uploaded to NRCan's Precise Point Positioning tool to determine an absolute base station coordinate referenced to NAD83 CSRS 2002.0. A rover unit (Fig. 1b) was used to survey locations of ground control points deployed in the field. Reflective 1 by 1 m

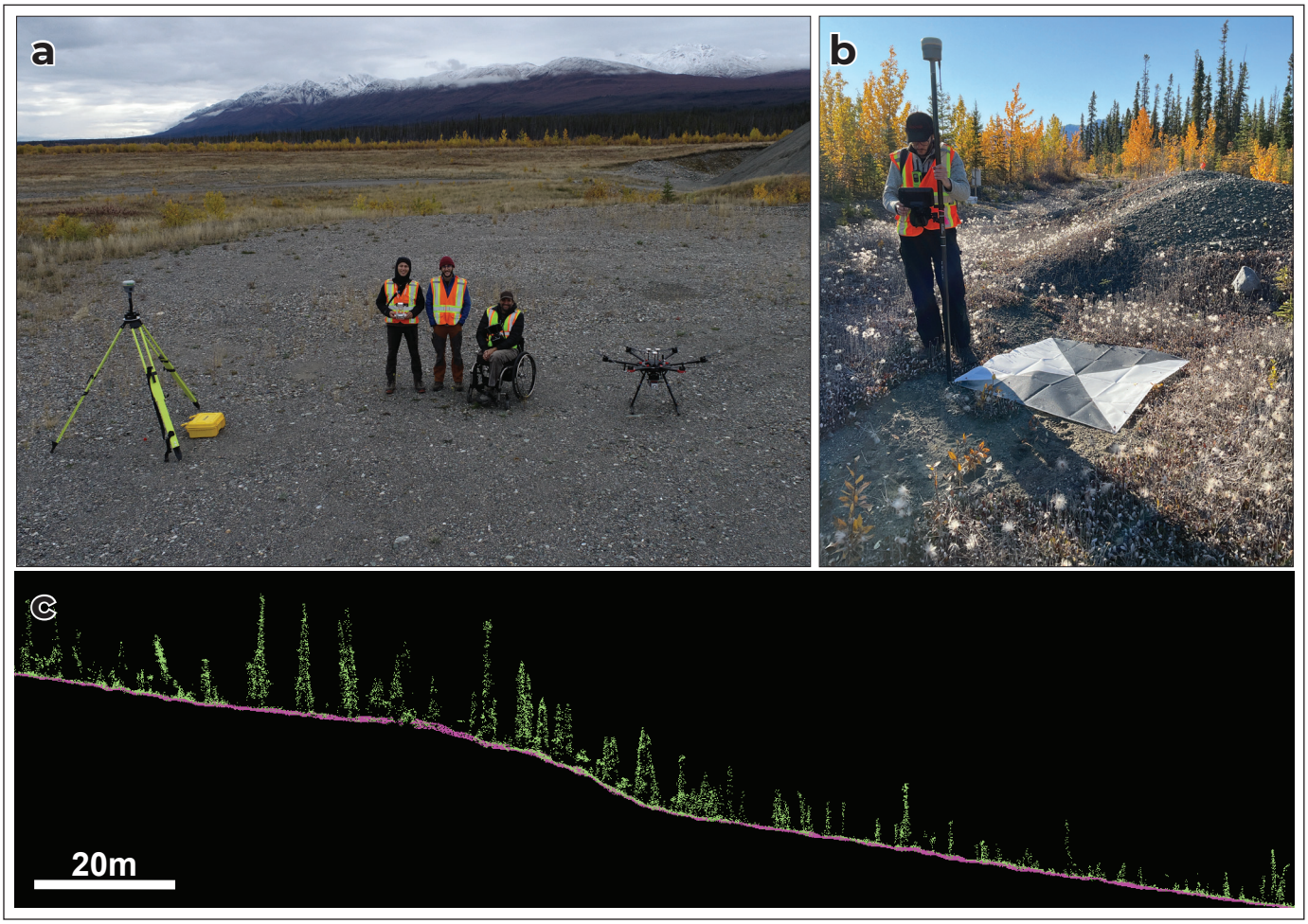

Figure 1. (a) *The field crew at launch site in gravel pit southeast of Duke River, with the DJI Matrice M600 drone, and RTK GNSS base station.* ***(b)*** *Collecting ground control point coordinates with the RTK rover unit and portable 1 m² fabric targets.* ***(c)*** *Lidar point cloud swath profile (5 m wide) across EDF scarp at Quill Creek. Points are coloured according to classification: ground (pink) and vegetation (green). Note that some points on the ground are coloured green, indicating the classification scheme could be improved.*

fabric squares with black and white quadrants were used as ground control targets (Fig. 1b). Following the field acquisition, rover acquired GNSS positions were calibrated and referenced to the base station absolute coordinates.

Trajectories acquired with the APX-20 GNSS-Inertial system were refined and post processed in single base mode with the Trimble GNSS base station using POSPac UAV. Laser data were processed using Riegl's RiProcess package. A rudimentary point classification was applied in RiProcess. As shown in Figure 1c the classification does not perfectly separate ground (pink) and vegetation (green) returns, and future efforts will focus on improving this classification. The resulting .las file was converted to a bare-earth DTM using a Triangular Irregular Network (TIN) algorithm in the LAStools software suite. Experimentation showed that a 30 cm pixel size was appropriate for the point density; attempts at finer resolution suffered from excess noise. The DTMs presented in this report are not final. Future efforts will focus on calibrating between individual flight lines, which do not currently align perfectly. Finally, the current data sets have not yet been adjusted with ground control points, so while they are relatively internally consistent, their spatial accuracy can be improved.

Survey Locations

Drone survey locations were selected and prioritized based on their scientific merit as well as the practical constraints of drone surveying, as discussed in the preceding section. The highest priority sites were located along the east and west sides of the Duke River, where geothermal drilling is to take place in the coming year. Secondary sites of interest were selected based on interesting features (e.g., potential offset markers) observed in existing satellite imagery that warranted closer examination. The regional map in Figure 2 shows the locations of the drone surveys in relation to one another along the EDF. In total, 4 km^2 of lidar data were acquired. A summary of each survey site follows.

Duke River Central (Surveys 1-3)

Three areas (Surveys 1–3) centred on the Duke River, collectively totaling 1.55 km^2, were surveyed over a period of 3 days (Fig. 3). An additional 0.19 km^2 survey (Survey 3a) was flown at half speed (3 m/s) to acquire higher resolution data over a subtle scarp feature on the abandoned river terrace. This topographic surface is likely younger than other locations where the fault is observed, and thus could constitute a tighter bound on the age of the most recent fault activity. The drone was launched from several open spots on the dirt road

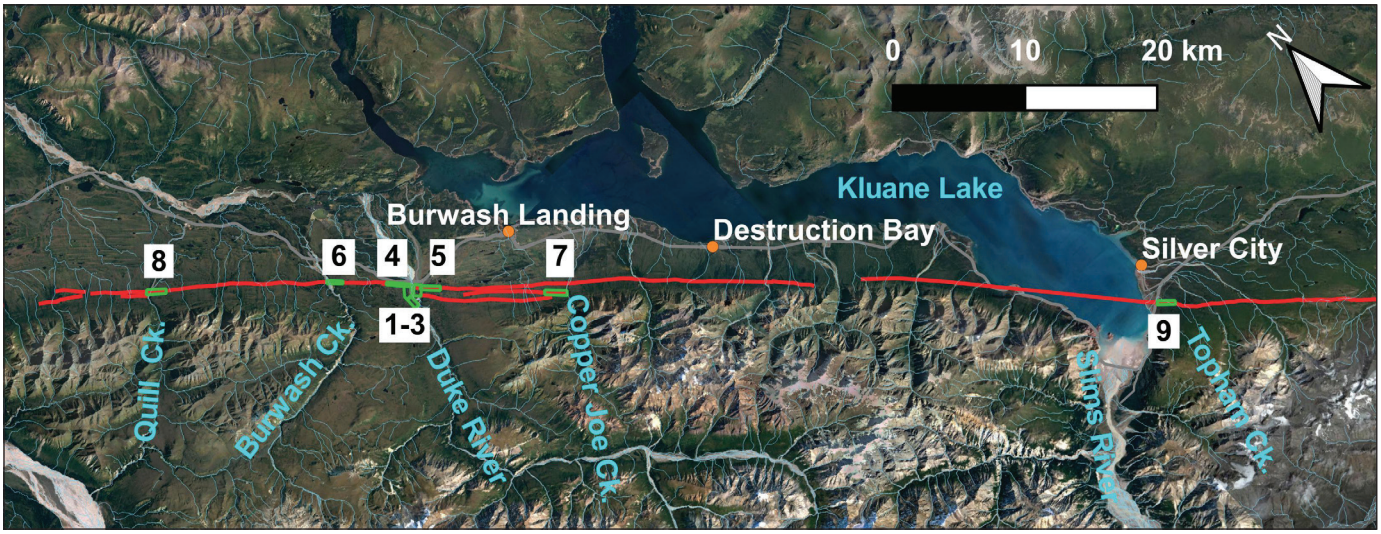

Figure 2. *Regional map of study area on southwest side of Kluane Lake. EDF surface trace (red line) is from Bender and Haeussler (2017). Numbered green polygons indicate the locations of high-resolution drone lidar acquisitions: 1–3. Duke River Central; 4. Duke River Northwest; 5. Duke River Southeast; 6. Burwash Creek; 7. Copper Joe Creek; 8. Quill Creek; 9. Topham Creek. See Figure 3 for detailed map of surveys 1–5, and Figure 4 for detailed maps of surveys 6–9.*

leading to the Donjek Route trailhead on the northwest side of the Duke River, and from two open meadows on the abandoned river terrace on the southeastern side of the Duke River. Visual observers were stationed in open meadows at the edges of the survey areas farthest from the launch sites to maintain constant VLOS. These survey areas were selected to cover the highest priority geothermal drill sites proposed by Witter (2020). The final selection for the geothermal test well is contained within Survey 1, and two other recommended sites are contained in Survey 3. Survey 2 was conducted to provide continuous lidar coverage from the known EDF fault trace (Survey 4) to the selected drill site (Survey 1). Based on ArcticDEM data, Witter (2020) suggested a possible secondary parallel strand of the EDF only 200 m northeast of the final drill site selection (Fig. 3). A critical goal of Survey 2 was to determine whether this fault strand disturbs the Holocene land surface, or whether the observed features are just glacial lineaments. The results of Surveys 1–3 are shown in Figure 5.

Duke River Northwest (Survey 4)

A linear swath totaling 0.42 km^2 was surveyed on the northwest side of the Duke River along the known trace of the EDF, requiring a half-day deployment (Fig. 3). The drone was launched from the broad ditch on the northeast side of the Alaska Highway and a visual observer was stationed on the southwest side of the EDF. This survey is immediately northwest along strike

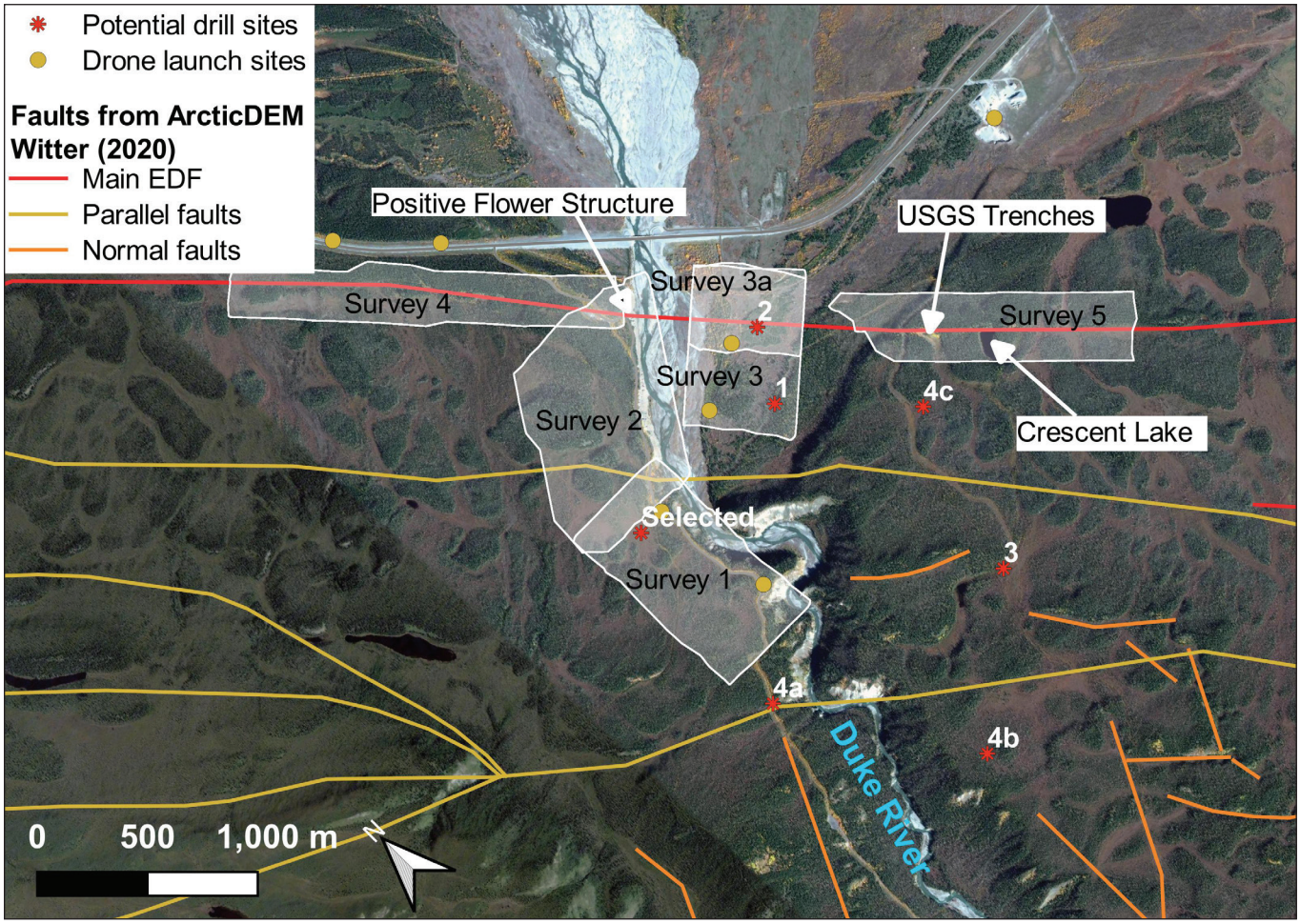

Figure 3. *Map of Surveys 1–5 (transparent polygons) in the vicinity of the Duke River. Faults interpreted by Witter (2020) are based on lineaments in ArcticDEM data. Preferred geothermal drill sites from Witter (2020) are also indicated with red dots. Locations of paleoseismic study sites discussed in Blais-Stevens et al. (2020) are labelled.*

from a positive flower structure that is bisected by the Duke River, as discussed by Blais-Stevens et *al.* (2020). The main goal of this survey was to cover sediment mounds along strike that are inferred to be similar structures. The results of Survey 4 are shown in Figure 6.

Duke River Southeast (Survey 5)

A linear swath totaling 0.39 km^2 was surveyed on the southeast side of the Duke River along the known trace of the EDF, requiring a half-day deployment (Fig. 3). The drone was launched from a Department of Highways and Public Works gravel pit on the southwest side of the Alaska Highway. Good sight lines from the launch site meant that no remote visual observer was necessary for this survey. This survey was designed to cover the highly studied segment of the EDF, where paleoseismic trenches and sediment cores from Crescent Lake have been used to infer up to 4 major earthquakes in the past 6000 years (Lipovsky et *al.*, 2009; Haeussler et *al.*, 2017; Blais-Stevens et *al.*, 2020). The results of Survey 5 are shown in Figure 7.

Burwash Creek (Survey 6)

An area of 0.37 km^2 was surveyed on the southeast side of Burwash Creek, 6 km northwest of the Duke River, requiring a half-day deployment (Fig. 4a). The drone was launched from a flat gravel area adjacent to a dirt road used by placer miners and a visual observer was stationed in the central part of the survey area to ensure VLOS. The intention of this survey was to capture the Denali fault at the nearest accessible location along strike from the central Duke River study area. Additionally, it appeared as though the fault crosses at least one abandoned terrace of Burwash Creek (Fig. 4a), which may provide some constraint on multi-event earthquake chronology. The results of Survey 6 are shown in Figure 8.

Copper Joe Creek (Survey 7)

An area of 0.43 km^2 was surveyed on the northwest side of Copper Joe Creek, 12 km southeast of the Duke River, requiring a half-day deployment (Fig. 4b). The drone was launched from a small gravel parking area at the trailhead for the Donjek Route. VLOS for the pilot

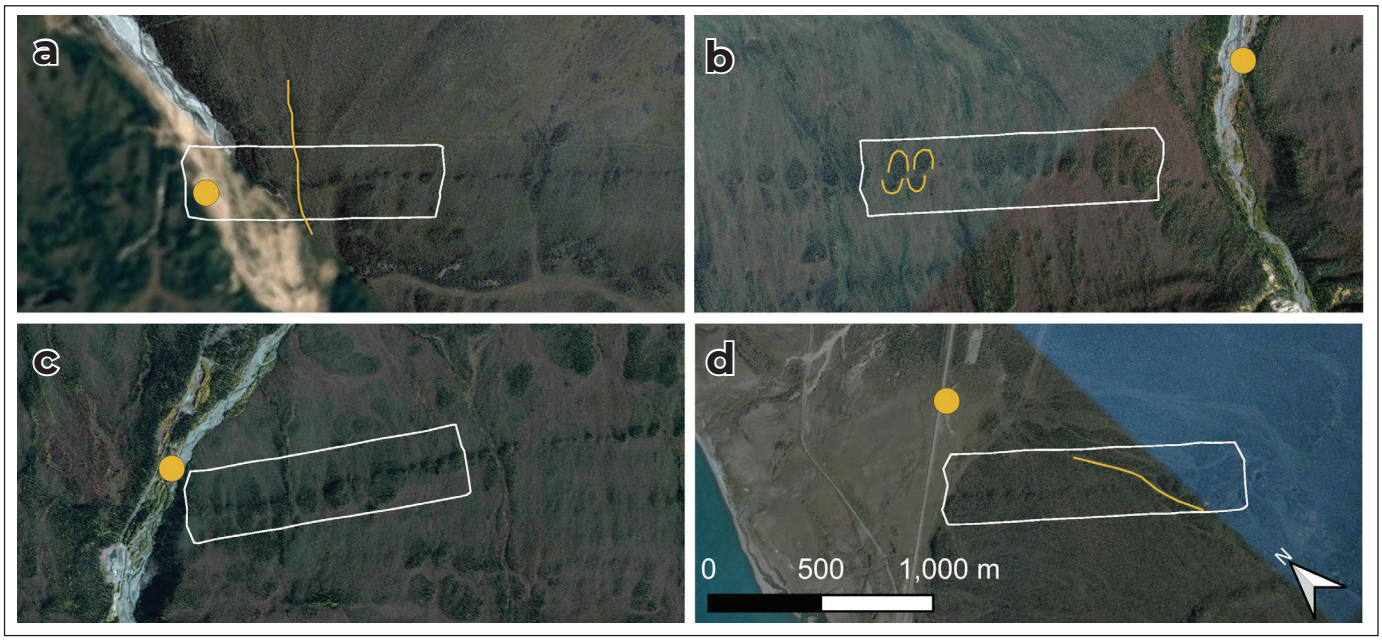

Figure 4. *Satellite imagery showing local context of Surveys 6–9. All maps are at the same scale and orientation. Yellow dots indicate drone launch sites.* ***(a)*** *Survey 6 on the southeast side of Burwash Creek. Yellow line shows possible edge of abandoned river terrace;* ***(b)*** *Survey 7 on the northwest side of Copper Joe Creek. Yellow lines show two offset mounds discussed by Haeussler et al. (2017) and Blais-Stevens et al. (2020);* ***(c)*** *Survey 8 on the southeast side of Quill Creek;* ***(d)*** *Survey 9 at the southeast end of Kluane Lake at Topham Creek. Yellow line shows trace of Topham Creek as it crosses the fault scarp.*

in command was challenging at this site due to a hill near the launch site blocking the view to the northwest, so a visual observer hiked approximately 1 km along the survey footprint to maintain visual contact with the drone. The primary goal of this survey was to capture lidar imagery of sediment mounds along the fault that have been interpreted in previous studies (Bender and Haeussler, 2017; Blais-Stevens *et al.*, 2020) as evidence of 20–30 m of dextral offset (Fig. 4b). The results of Survey 7 are shown in Figure 9.

Quill Creek (Survey 8)

An area of 0.39 km^2 was surveyed on the southeast side of Quill Creek, 20 km northwest of the central Duke River study area, requiring a half-day deployment (Fig. 4c). The drone was launched from a gravel pull out adjacent to a prospector's cabin on the northwest side of the river. A large hill halfway along the survey swath obscured the view of the farthest extent of the survey, so a visual observer hiked to this location to maintain VLOS. This site was chosen to extend our survey coverage as far to the northwest as was practically possible within this field season. Additionally, this fault segment strikes ~10° more westerly than the other segments and appears to have a distinct right-stepping bend highlighted by a large grove of Black Spruce (Fig. 4c). The results of Survey 8 are shown in Figure 10.

Topham Creek (Survey 9)

An area of 0.41 km^2 was surveyed at the southeast end of Kluane Lake adjacent to Topham Creek, 56 km southeast of the Duke River study area, requiring a half-day deployment (Fig. 4d). The drone was launched from a flat gravel area on the south side of the Alaska Highway. This is the farthest southeast location where the EDF trace is both accessible and clearly observable in satellite imagery; obtaining measurements here is important for understanding the size and length of past surface ruptures. Additionally, this is one of few locations where the fault climbs significantly in elevation along-strike, which may help with measuring 3D fault offset. Finally, Topham Creek crosses the fault at an oblique angle here and we speculated it might be used as a displacement maker (Fig. 4d). The results of Survey 9 are shown in Figure 11.

Results and preliminary interpretations

Duke River Central Area (Surveys 1–3)

Likely owing to ease of access, the central Duke River area is one of the most thoroughly studied sections of the EDF, and is featured in papers and reports by Clague (1979), Seitz *et al.* (2008), Lipovsky *et al.* (2009), Witter (2020) and Blais-Stevens *et al.* (2020). Nevertheless, lidar data do provide some new insight for this area. Most notably, the fault makes a distinct 7° right-stepping bend as it crosses the low-lying abandoned river terrace on the southeastern side of the Duke River (Fig. 5). This right-stepping bend likely represents a releasing bend in a dextral system, and although it was identified by Witter (2020) in ArcticDEM data, the lidar data allow for a more accurate determination of the true geometry. The red dots in Figure 5 indicate discrete inflection points where the fault changes strike. Also noteworthy here is the fact that the fault scarp on the abandoned river terrace is sharper and narrower than the fault trace to the east and west (Fig. 5 inset). Vertical separation is less than 2 m, down to the northeast. The sediment mounds that characterize the majority of the EDF elsewhere along strike are non-existent on this short segment. This segment is one of very few places along the fault where a scarp is observed deforming a young fluvial surface, as opposed to an older glacially-affected surface. Furthermore, there appears to be a stream channel offset by 5–10 m across this scarp (Fig. 5 inset), which is smaller than dextral offsets measured elsewhere along strike. It may be that the fault scarp here records only the youngest rupture event, whereas the larger more complex fault traces elsewhere represent multiple ruptures. The lack of sediment mounds and the slight change in strike is consistent with this segment undergoing oblique dip-slip faulting to accommodate localized extension in this dextral releasing bend.

The lidar data also allow for definitive classification of other lineaments as non-tectonic. Witter (2020) used ArcticDEM data to trace out potential parallel strands of the EDF. One of these lineaments is indicated with the white arrows in Figure 5. This feature does appear to be a southwest-side-up terrace of some sort, but there is not a distinct fault scarp observed in the lidar here.

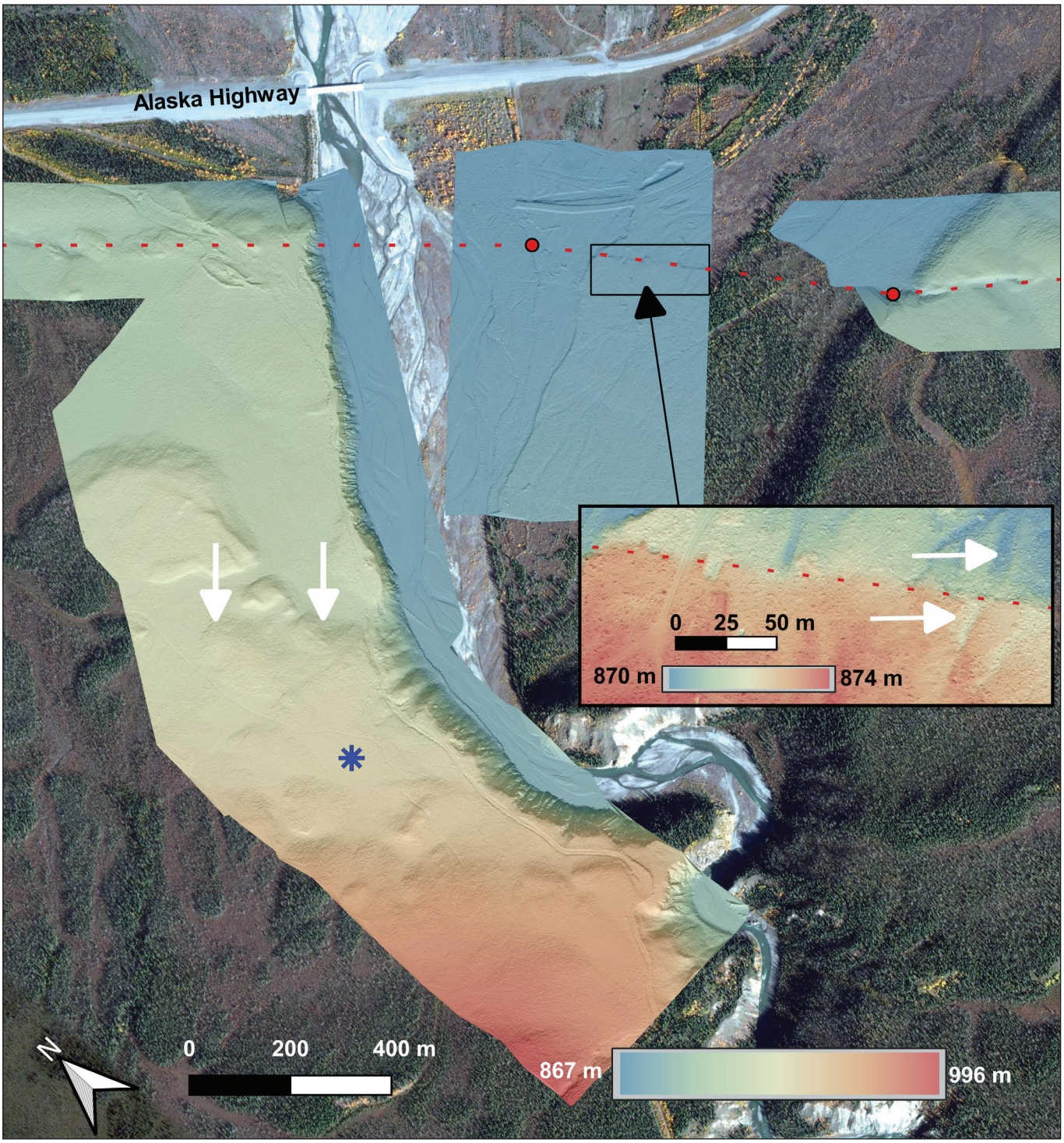

Figure 5. *Lidar hillshade (30 cm resolution) of the central Duke River study area (Surveys 1–3 and parts of 4 and 5). Dashed line shows the surface trace of the main strand of the EDF. Red dots indicate inflection points where the fault makes a discrete 7° right-stepping bend to form a possible releasing bend. White arrows indicate a feature interpreted by Witter (2020) as a Holocene fault scarp. The blue star shows the chosen drill site, 1 km southwest of the main EDF. Inset hillshade shows detail of fault scarp at 10 cm resolution (Survey 3a) where it crosses abandoned river terrace; white arrows indicate possible 5–10 m dextral offset in old stream channel at southeast end of inset.*

If this lineament is a fault scarp it is much older than the main trace of the EDF, having had time to become eroded and more diffuse.

The selected geothermal drill site is shown with the blue star in Figure 5. It is approximately 1 km southwest of the main strand of the Denali fault. The lidar data indicate there are no Holocene fault scarps in the immediate vicinity of the drill site. However, while in the field, we examined the cliffs on the northwest side of the Duke River immediately below a topographic bench interpreted as a fault by Witter (2020). In the cliff, there does appear to be a significant bedrock fault that coincides with this topographic feature, but it is unclear whether it breaks through into unconsolidated Late Quaternary sediments. These observations (which will be reported in more detail in subsequent reports), and mapping of numerous bedrock faults in the canyon walls of Burwash Creek by Witter (2020) together indicate that the EDF is a broad fault zone, with only one strand currently active and visible in lidar. The older strands that do not have apparent Holocene surface ruptures, may still be permeable to hydrothermal fluid.

Duke River Northwest (Survey 4)

The fault scarp is subdued and relatively narrow at the Duke River Northwest site (Fig. 6). There does not appear to be any consistent sense of vertical separation across the fault in this survey area. A series of small sediment mounds occur along the fault trace here. These mounds are roughly 40 by 40 m (smaller than many other mounds observed along strike). We interpret these mounds to represent en echelon push-ups (Fig. 6 inset), or "mole tracks" which are often associated with large strike-slip displacements (Little *et al.*, 2021).

Duke River Southeast (Survey 5)

The fault scarp is very distinct at the Duke River Southeast site (Fig. 7). This survey covers the locations of three paleoseismic trenches excavated by Seitz *et al.* (2008) and revisited by Blais-Stevens *et al.* (2020). Crescent Lake, from which sediment cores were retrieved and studied by Blais-Stevens *et al.* (2020), is also covered. This segment of the fault is northeast-side-up, with a vertical separation in the range of 3–8 m. Although not fully covered by the drone survey, the old riverbank at the northwestern end of the survey appears to be dextrally offset by 30–40 m. On the northeast side of the fault, a regular pattern of east-west trending lineations repeated on an ~5 m wavelength appear on the outer edge of broad mounds (Fig. 7 inset). These features are not simply artifacts of the hillshade effect and appear regardless of light source azimuth. These may record north-south compression in the surficial sediments, though it is also possible they are related to frost slumping. They

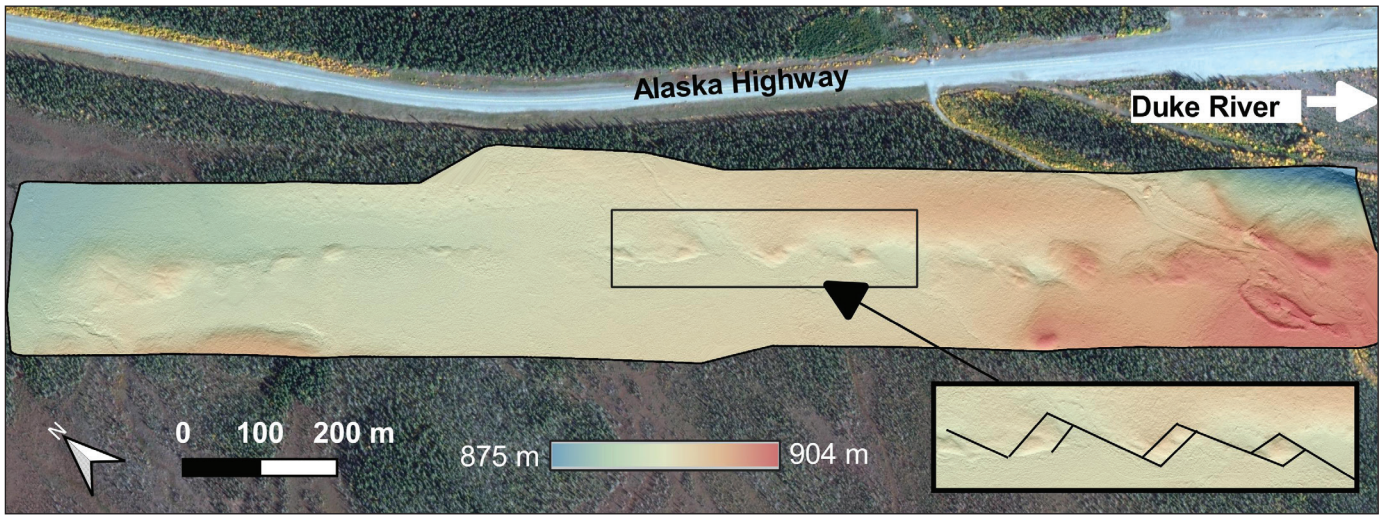

Figure 6. *Survey 4 lidar hillshade (30 cm resolution) of the EDF on the northwestern side of the Duke River. Inset shows possible interpretation of sedimentary mounds as en echelon positive flower structures.*

will be more thoroughly investigated as possible strain recorders in future work. It is worth noting that these features would not be easily discerned in typical 1 m resolution airborne lidar.

Burwash Creek (Survey 6)

The fault scarp at Burwash Creek (Fig. 8) is moderately distinct in the landscape, although the surface expression in the northwestern part of the survey area is obscured by the braided river channel and recent placer mining excavations on the riverbanks. At this site, the fault scarp does not have distinct vertical separation, although the fault trace itself is characterized by several sediment mounds. The curvature of the hill in the southwestern corner of the survey appears to be dextrally offset, but this is an imprecise marker. Similar to Survey 5, linear east-west structures are observed on the northern slopes of the sediment mounds (Fig. 8 inset). It is possible these are related to freeze-thaw cycles on north-facing slopes, but if so, it is difficult to understand why they occur at oblique angles (45°) to the slope dip direction in most cases.

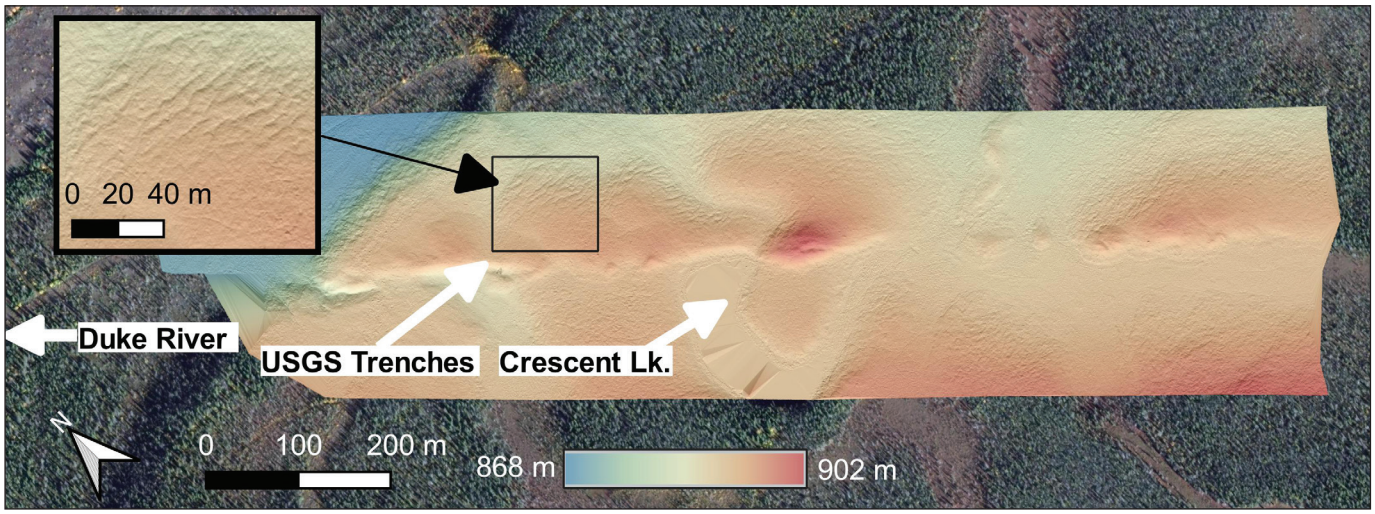

Figure 7. *Survey 5 lidar hillshade (30 cm resolution) of the EDF on the southeastern side of the Duke River. Locations of the USGS trenches and Crescent Lake (discussed by Blais-Stevens et al. (2020)) are indicated. Inset shows east-west trending fold-like structures.*

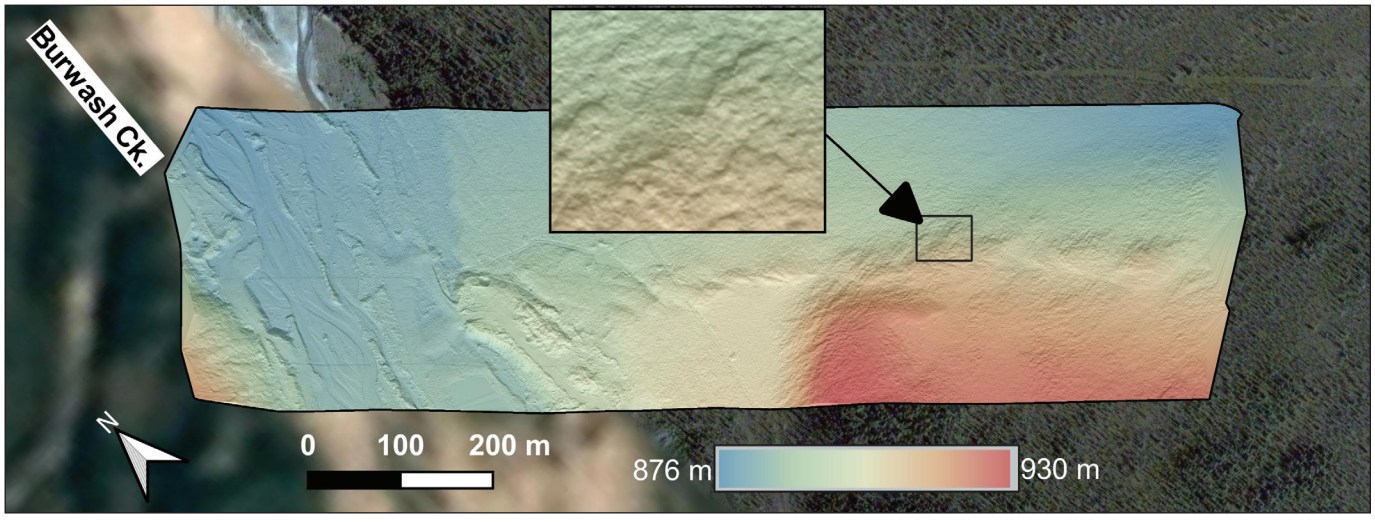

Figure 8. *Survey 6 lidar hillshade (30 cm resolution) of the EDF on the southeastern side of Burwash Creek, 13 km northwest of Burwash Landing. Inset shows east-west trending lineations.*

Copper Joe Creek (Survey 7)

Despite being quite distinct in satellite imagery, the fault scarp at Copper Joe Creek is not very distinct in the lidar hillshade (Fig. 9). The strike of the fault appears variable, and it is not clear if there is any vertical separation. The pair of mounds at the northwestern end of the survey are the same pair of mounds from which Haeussler et *al.* (2017) estimated a dextral offset of 22.5 +7.5/–2.5 m. It may be possible to derive a more accurate estimate of offset from the lidar data, however, with the vegetation stripped away, the boundaries of these markers actually become less distinct than the Black Spruce groves visible in satellite imagery (Fig. 4b). Notably, no other mounds in this survey area appear to be offset by the fault trace. It may be that the apparent offset of the Black Spruce groves is deceptive and there is not actually any discrete offset between the mounds; rather, the mounds may just be coincidentally shaped in a way that gives the illusion of offset. If the mounds are offset, they must record multiple earthquake ruptures: at least one to have formed them in the first place, and probably at least two more to achieve such large lateral separation. In the southeastern end of the survey area, the fault appears to make a 100 m right-stepping bend, which may represent a releasing bend. Similar to Surveys 5 and 6, a series of ~5 m wavelength east-west trending lineations appear on the north slopes of the sediment mounds (Fig. 9 inset).

Quill Creek (Survey 8)

The fault scarp at Quill Creek is very distinct in the lidar hillshade (Fig. 10). It is consistently southwest-side up, with a vertical separation of 8–16 m. The southeastern part of the surveyed fault segment is characterized by a series of 10 distinct en echelon mounds with their long axes oriented east-west, and short axes oriented north-south. The northwestern part of the survey area has mounds, but they are less distinct. The largest mound, in the centre of Figure 10, is ~100 × 120 m and rises 20 m above the down-dropped (northeastern) side of the fault. This mound corresponds to a distinct left-stepping bend in the fault and is therefore likely a restraining bend/positive flower structure (Fig. 10 inset). The northern slope of this mound exhibits east-west trending lineations similar to those observed in previous surveys.

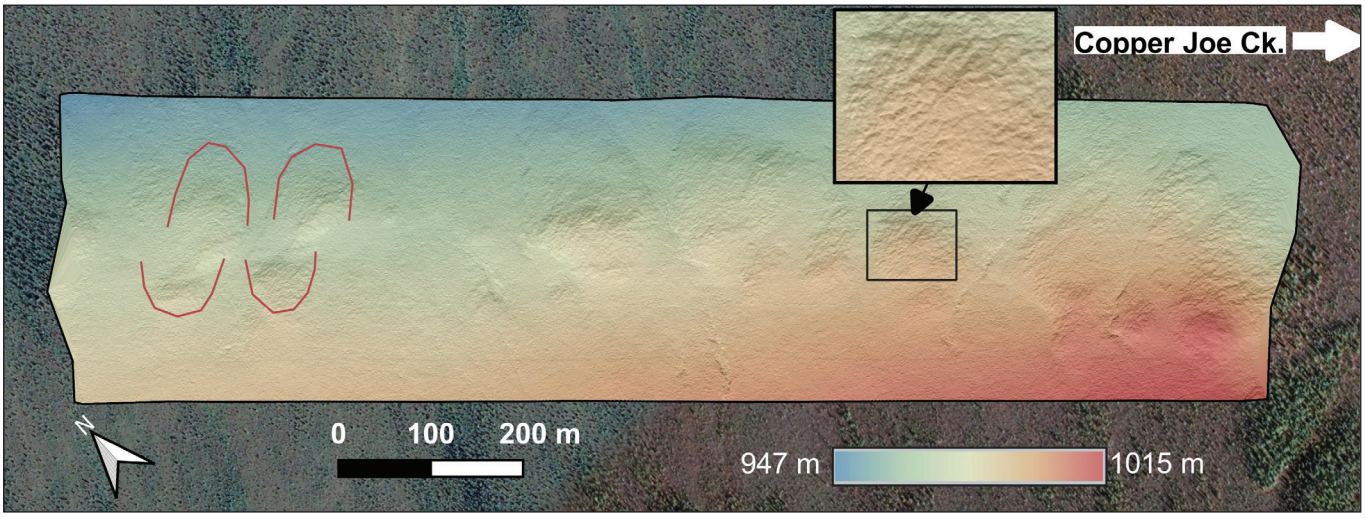

Figure 9. *Survey 7 lidar hillshade (30 cm resolution) of the EDF on the northwestern side of Copper Joe Creek, 5 km south of Burwash Landing. Pink lines show outlines of possible offset mounds discussed in Haeussler et al., (2017) and Blais-Stevens et al. (2020). Linework is based on the boundaries of Black Spruce groves, as the boundaries of the mounds are less distinct. Inset shows detail of east-west lineations visible on north sides of all sedimentary mounds, similar to Survey 5 and 6.*

Topham Creek (Survey 9)

The fault scarp at Topham Creek is very distinct in the lidar hillshade (Fig. 11). It is consistently southwest-side up, with a vertical separation of approximately 8–12 m. Where Topham Creek crosses the fault scarp, it deviates course by ~20°. This channel offset is suggestive of dextral displacement up to a maximum of 75 m. However, due to the oblique angle at which the stream intersects the fault, obtaining an good estimate of offset is challenging; software tools such as LaDiCaoz (Zielke and Arrowsmith, 2012) or 3D Fault Offsets (Stewart et *al.*, 2018) may be appropriate for obtaining more accurate measurements of displacement.

Discussion

Fault kinematics and displacement

Compared to previously available DEMs of the EDF, the drone lidar data allow for much higher-confidence estimations of kinematics and fault displacement from geomorphological features (Fig. 12). Lateral offsets observed in multiple surveys and the geometry of the "mole tracks" all consistently indicate dextral slip. The amount of apparent dextral slip varies from a minimum of 5 m at the Duke River abandoned river terrace to 75 m at the Topham Creek site.

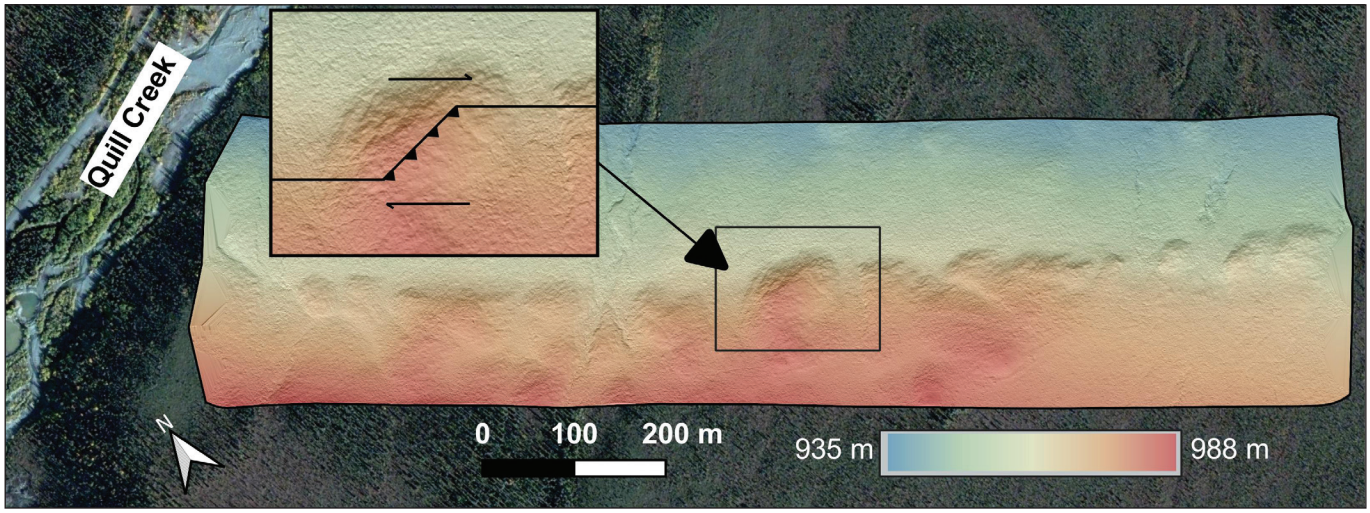

Figure 10. *Survey 8 lidar hillshade (30 cm resolution) of the EDF on the southeastern side of Quill Creek, 27 km northwest of Burwash Landing. Inset shows interpretation of large sediment mound as a restraining bend.*

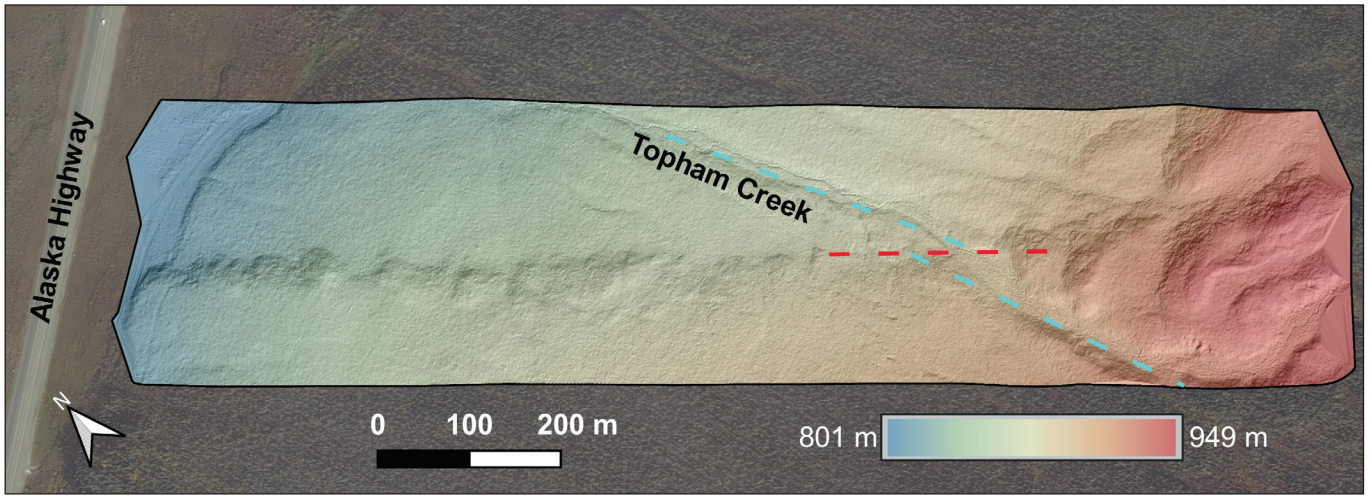

Figure 11. *Survey 9 lidar hillshade (30 cm resolution) of the EDF at Topham Creek near the southeastern end of Kluane Lake. Red dashed line is the approximate trace of the fault; cyan dashed lines are the offset projections of Topham Creek channel on either side of the fault, indicating a possible dextral offset of ~75 m.*

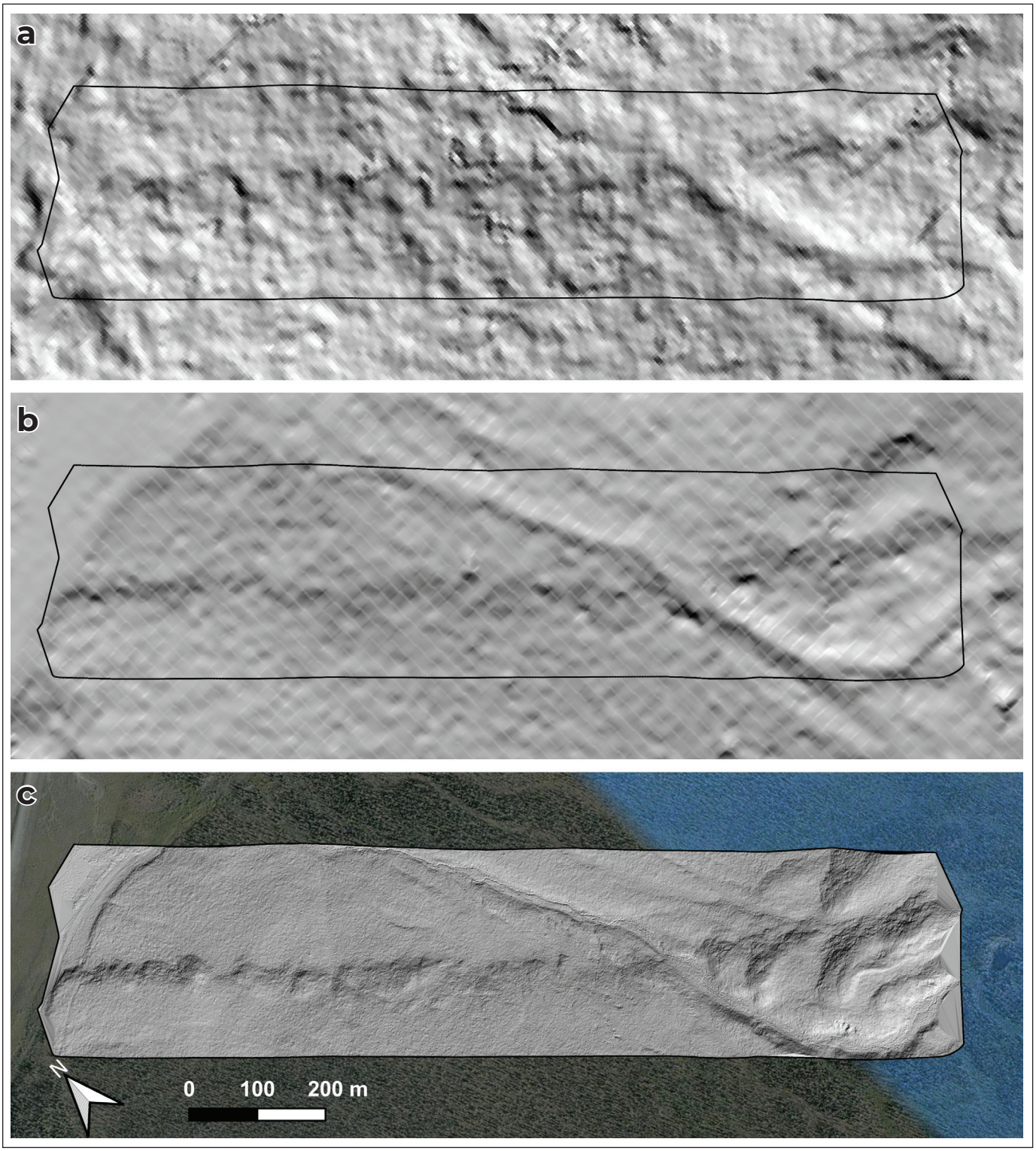

Figure 12. *Comparison between the drone lidar DTM from this study and DSMs from which previous maps and interpretations of the EDF have been made. All panels are the same scale and orientation at the Topham Creek site (Survey 9).* ***(a)*** *The 4 m photogrammetric DSM hillshade produced from air photos by Bender and Haeussler (2017).* ***(b)*** *The 2 m ArcticDEM hillshade produced from optical satellite imagery by Porter et al. (2018).* ***(c)*** *30 cm DTM produced by our lidar drone platform.*

If these offsets are valid, the larger ones likely record multiple earthquake ruptures, while the smaller ones on younger fluvial surfaces may only record a single rupture. Vertical separation is more variable, ranging among no separation, <2 m to 20 m of southwest-side-up separation at Duke River, Quill Creek and Topham Creek, and 3–8 m of northeast-side-up separation at Duke River Southeast. The variability of vertical separation along strike supports the notion that rupture on the EDF is predominantly strike-slip. Several features, in particular the offset channel of Topham Creek (Fig. 11), the offset sediment mounds at Copper Joe Creek (Fig. 9), and the offset river channel on the abandoned Duke River (Fig. 5 inset), may allow for accurate estimates of three-dimensional fault displacement using software tools such as LaDiCaoz (Zielke and Arrowsmith, 2012) or 3D-Fault-Offsets (Stewart *et al*., 2018).

The high spatial resolution of the drone lidar is also useful in allowing an improved understanding of the structure of the somewhat enigmatic sediment mounds which occur along the fault trace. It is apparent that in many places these mounds have a preferred east-west orientation to their long axes (*e.g.*, Quill Creek segment, Fig. 10). In many cases, there are east-west-trending lineations on the northern slopes of these sediment mounds; we tentatively interpret these as folds or fault tips resulting from north-south compression across these mounds. However, more work, including ground-truthing in the field will be required to confirm a tectonic cause. They instead could be caused by slumping due to freeze-thaw cycles on north-facing slopes, but if so, it is unclear why they are often oriented oblique (~45°) to the slope fall line (*e.g.*, Fig. 8). They are not an artifact of the hillshade effect and are visible at a variety of light source azimuths. It is worth noting that these features would not be easily discerned in traditional 1 m resolution lidar data, so if they are records of strain, the utility of high-resolution drone lidar is clear. However, more work is required to prove their origin definitively.

Width and complexity of the EDF

At the central Duke River study site, the combined areas of Surveys 1–4 cover ground up to 2 km from the main EDF trace. In this area, the lidar data do not reveal any parallel splays of the main EDF as originally interpreted by Witter (2020), indicating that strain on this segment is concentrated to one fault plane. Given that complex faults with wide damage zones and high fracture density are generally more permeable to fluid flow (Caine *et al*., 1996), this finding suggests hydrothermal circulation may be limited. However, preliminary mapping by ourselves and by Witter (2020) found evidence for multiple significant bedrock faults in the Burwash Creek and Duke River canyons; although these faults do not appear to rupture to the surface, or at least not to the degree required to generate clear topographic expressions, they still may be relatively young: for example McDermott *et al.* (2021) obtained Pliocene ages from EDF fault surfaces using hematite thermochronometry.

The amount of off-fault deformation at the surface varies along strike. The width of the zone of clearly deformed sediments varies from ~2 m (Duke River; Fig. 5 inset) to >100 m (Copper Joe Creek; Fig. 9 inset). This may reflect changes in bedrock fault zone dimensions along strike, or it may simply reflect the depth and type of Late Quaternary sediment through which the fault has ruptured. For example, a wider zone of deformation may be indicative of a deeper layer of sediment, in which deformation becomes more diffuse towards the surface. Alternatively, the width of the deformed zone of sediment may be a proxy for the amount of Late Quaternary slip that has been accommodated along that particular segment (*i.e.*, the gravel on the abandoned river terrace at Duke River has potentially only experienced one rupture event).

Fault geometry and geothermal favourability

Projecting the traces of the EDF scarps from either side of the Duke River shows that the fault makes a 7° right-stepping bend, and the fault trace shifts ~100 m laterally. Considering the ample evidence for dextral kinematics, this right-stepping bend is interpreted as a releasing bend with a component of localized extension. In the structurally controlled geothermal systems of Nevada, zones with localized extension tend to be more permeable to hydrothermal fluid flow. The selected drill site is approximately 1 km to the west of the fault bend, and it is unclear whether extensional strain would have an effect at that distance.

Stepovers can also be identified at other survey sites. The Quill Creek segment has a distinct 100 m left-stepping bend, which is interpreted to be a restraining bend giving rise to an exceptionally large sediment mound. The Copper Joe Creek segment appears to have a right-stepping bend, which may represent another local zone of extension. The proximity of the Copper Joe site to Burwash Landing makes this another potential candidate for geothermal energy extraction.

Future Work

These data and interpretations are preliminary, and further data collection and analysis will occur over the coming months and years. The following sections describe planned and suggested future work.

Improvement to the drone system

The use of a lidar-equipped drone for fault mapping is novel, and this deployment pushed the system to its limits in terms of flight time and distance from launch point. The data from the system are already useful, but the utility of the system would be even greater if the drone could fly for longer distances. There are several ways the flight distance could be improved, including:

- Mounting a small camera to the airframe to provide a real-time video feed to the pilot in command. This addition would allow for improved situational awareness when the drone is far from the launch point and the flight direction is difficult to discern.
- Upgrading the batteries. DJI does manufacture higher capacity batteries, but these would not be allowed in standard air cargo, limiting the deployment of the drone to locations within driving distance of the University of Victoria.
- Using a larger generator for recharging. In 2021 we used a 1000-watt generator, which was only capable of charging one set of batteries at a time. For future fieldwork we could reduce inefficiency by using a generator with higher wattage.
- Packaging the drone system appropriately to allow for transport via an ATV to more remote launch sites. In 2021 we were limited to launch sites accessible with a truck.
- Applying for Special Flight Operations Certificate (SFOC) from Transport Canada to allow for controller hand-off between multiple pilots stationed along a flight line. This allowance would enable a much longer survey, without requiring beyond-visual line-of-sight flight. Currently, such a system requires a bespoke control system not commercially available.
- Applying for an SFOC from Transport Canada to allow for beyond-visual-line-of-sight flight. This allowance has thus far only been granted to a handful of commercial operators. Furthermore, operating beyond visual line of sight would require a high degree of trust in the flight programming software, which currently experiences enough glitches to render it untrustworthy. Considering the cost of the drone system, and high consequences of a crash, considerable testing would be required before implementing such a high-risk flight.

Additional drone lidar acquisition

The preliminary results presented in this report show that the 3 to 10-fold increase in resolution achieved with the drone lidar as compared to traditional fixed-wing lidar, is useful for mapping fault structure in this particular region. Permanent strain recorders such as laterally-offset stream channels, and possible compressional structures in sediment mounds, would be barely-discernible, or at least less convincing, in traditional lidar, but are easily mapped with drone lidar. We propose collecting more drone lidar data at exposures of the EDF we were unable to cover in 2021. This includes filling in gaps in the data coverage at existing study sites and expanding coverage to the northwest and southeast. In addition to fault-parallel surveys, we suggest collecting several swaths perpendicular to the main fault to ascertain whether or not other lineaments in the hillside represent Holocene fault scarps.

Figure 13 shows proposed sites for additional coverage and the access considerations and scientific justifications are presented in Table 1. The highest priority sites (5–10 in Fig. 13) are proximal to the proposed geothermal site. More distant sites will be

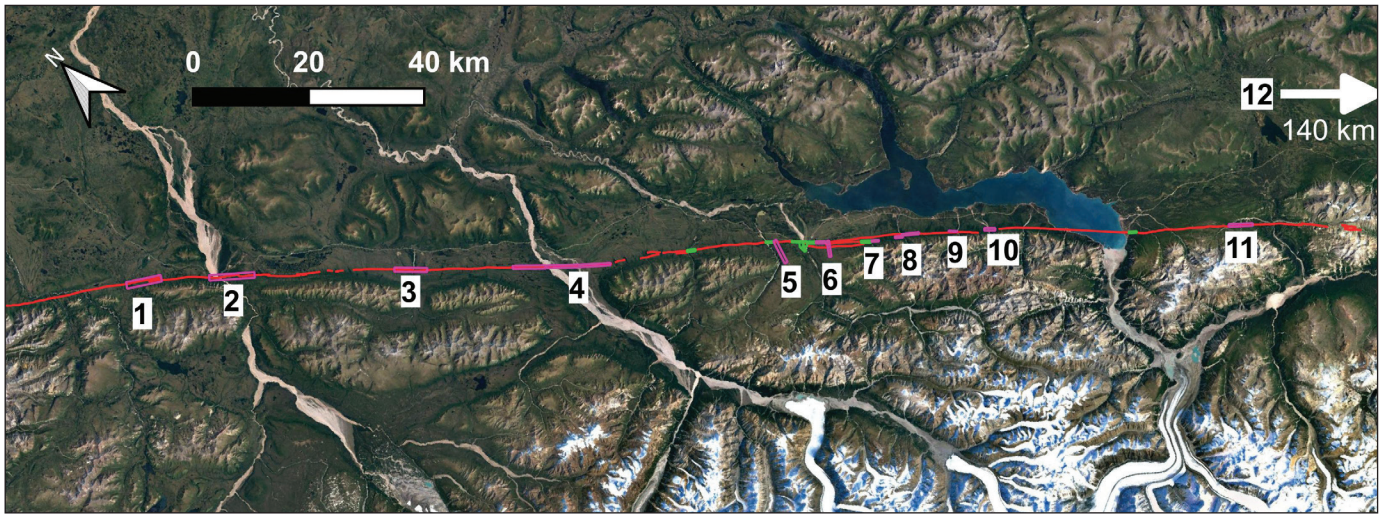

Figure 13. *Proposed locations (pink rectangles) for future drone lidar acquisition along the EDF. Green rectangles show areas captured in the present study. Numbers correspond to entries in Table 1.*

Table 1. *Proposed future study sites, access routes, and scientific justification.*

No.	Location	Access Route	Reason
1	Sanpete Creek	Road and ATV track	Farthest NW, close to US border; Several creeks with possible lateral offset.
2	White River	Adjacent to highway	Possible knickpoint in river; Unusual undulatory fault geometry.
3	Koidern River	Road on NW side of river	Possible disturbance of abandoned river terrace.
4	Donjek River	ATV tracks on river bars	Fault at high angle to local glacial lineations (possible offset markers); Possible disturbance of abandoned river terrace.
5	Burwash Creek Cross Profile	Road on NW side of creek	Distinguish any parallel fault splays (4 were identified by Witter (2020)).
6	Duke River Cross Profile	Dept. of Highway's Gravel Pit	Distinguish any parallel fault splays (3 were identified by Bender and Haeussler (2017)).
7	Copper Joe Southeast	Road on SE side of creek	Possible continuation of fault not identified by Bender and Haeussler (2017).
8	Lewis Creek	ATV up gravel creek bed?	Suspected deviation from EDF fault map created by Bender and Haeussler (2017).
9	Bocks Creek	Road and ATV track	Suspected deviation from EDF fault map created by Bender and Haeussler (2017).
10	Nines Creek	ATV track up creek bed	Possible disturbance of abandoned river terrace.
11	Telluride Creek	ATV/hiking route up Mt. Cairnes	Farthest accessible exposure of EDF mapped by Bender and Haeussler to SE.
12	Chilkat Pass	Adjacent to Haines Highway	Site of 2017 earthquake doublet (Choi *et al.*, 2021). Possible scarp/lineament observed in satellite imagery.

of more use for understanding the regional tectonics of the EDF. Many of the proposed future sites will be challenging to access via road, and may require the use of an ATV to transport the drone system to a suitable launch site.

Field studies and ground truthing

Witter (2020) documented multiple bedrock faults in the cliffs along Burwash Creek and Duke River. Future effort should be undertaken to map these faults in detail, including their widths, kinematic indicators, and whether they disturb unconsolidated Quaternary sediments that drape over top of them. Although there is no clear evidence in lidar data that these faults disturb the surface, this does not rule out a Quaternary age; it may be possible to observe disturbed Quaternary sediments in cross section, even if the surface trace is muted. Furthermore, mapping out the fault zone architecture (*i.e.*, damage zone and fault core) will help constrain fault zone permeability.

The east-west lineations observed on the north slopes of the sediment mounds also need to be investigated in the field. Given their subtle nature, they were not obvious on the ground during 2021 fieldwork. It may be possible to excavate a shallow trench across them to view a cross section of their internal structure. Additionally, it would be worth searching for similar features on slopes not adjacent to the EDF. If they are ubiquitous on north facing slopes in the area, they likely all have a non-tectonic origin.

Slip and dilation tendency modeling of the 2D fault map

In addition to drone surveys and fieldwork, we plan to conduct kinematic modeling based on the detailed lidar-derived fault map. Earthquake focal mechanisms will be used to estimate stress directions and magnitudes using a Bayesian stress inversion (e.g., Balfour et *al.*, 2011). Ristau et *al.* (2007) conducted this sort of analysis for earthquakes in western Canada with M_w>4, but an additional 14 years of seismicity could be added to the catalog to further refine our understanding of the regional stress field. The recent addition of data from the Earthscope Transportable Array in Alaska and across the Mackenzie Mountains (Baker et *al.*, 2019; Busby and Aderhold, 2020) will greatly improve focal mechanism determinations in the region. Choi et *al.*, (2021) relocated earthquakes and determined stress directions using focal mechanism inversions along the southern section of the EDF, but a similar reanalysis has not yet been conducted in the vicinity of the geothermal drill site. The detailed fault maps obtained with the lidar drone (or future airplane) will be integrated with seismological stress axes and other data sources to model kinematics on the EDF. Specifically, slip and dilation tendency will be calculated for fault segments identified in lidar imagery. Slip tendency (T_S) is the likelihood of a fault to slip in a certain stress field, and is quantified as the ratio between shear stress (τ) and normal stress (σ_n) relative to the friction coefficient of the rocks (μ_s):

$$T_S = \frac{\tau}{\sigma_n} \geq \mu_s$$

Dilation tendency (T_D) is controlled by the relative orientation of the maximum and minimum compressive stresses (σ_1 and σ_3) and normal stress (σ_n) acting on a fault plane; when the normal stress is parallel to the principal stress, the dilation tendency will be 0, and when the normal stress is parallel to the minimum stress, dilation tendency will be 1:

$$T_D = \frac{\sigma_1 - \sigma_n}{\sigma_1 - \sigma_3}$$

The tendency of a fault to slip or dilate is a proxy for permeability, and this technique has been used to aid in drill-targeting at numerous fault-controlled geothermal systems around the world (e.g., Moeck et *al.*, 2009; Jolie et *al.*, 2015; Meixner et *al.*, 2016, 2018).

Currently, the subsurface geometry of the EDF is only roughly constrained. Lidar imagery will refine surface maps of the fault trace, and while this is useful, other geophysical techniques will be necessary to properly model subsurface structure and kinematics. Seismicity patterns (from relocation algorithms), and geophysical data (e.g., EM, seismic tomography, gravity, magnetics) obtained as part of the YGS's geothermal project, could provide a more detailed view of subsurface fault

geometry, and thus inform kinematic modeling. Existing regional geophysical surveys of the Yukon may also help with this task. However, even with poorly constrained subsurface geometry, the slip and dilation tendency can be modeled for a range of dip angles given high resolution fault segment mapping on the surface (*e.g.*, Meixner et *al.*, 2018).

Conclusion

The preliminary results presented in this report demonstrate the utility of high-resolution drone lidar for active fault mapping. We were able to: 1. map fine scale fault geometry that could be conducive to hydrothermal fluid flow, and 2. improve constraints on the kinematics and rupture magnitude of prehistoric earthquakes on the EDF, both of which are important factors for developing fault-hosted geothermal systems. The bare-earth DEMs and hillshades derived from the lidar point clouds are three times the resolution of traditional fixed-wing lidar and allow for much higher resolution mapping of the EDF surface trace than was possible with existing photogrammetric DEM products (*e.g.*, Bender and Haeussler, 2017). The overall cost of deploying the lidar drone is a fraction of traditional airborne lidar systems, although airborne systems are more efficient at covering a much larger area. The true utility of the drone system is its ability to target known fault segments with very high spatial resolution. We observe subtle strain markers such as offset channels and deformed surface sediments that can be used to estimate kinematics and slip magnitudes of past ruptures. We can resolve small restraining and releasing bends, some of which were not previously mapped; the releasing bends are considered conducive for hydrothermal fluid circulation. In the future, we will use these data to perform slip and dilation tendency modeling of the EDF but recommend that more drone lidar data be acquired in subsequent field seasons. Additionally, structural mapping of bedrock faults in drainages crossing the EDF will help to elucidate the relationship between the recent ruptures, and older faulting.

Acknowledgements

Excellent food, lodging and research infrastructure was provided by the Kluane Lake Research Station/ Arctic Institute of North America. Special thanks to Harry Penn for accommodating our myriad of requests. Funding and logistical support was provided by the Yukon Geological Survey. Sincere thanks are due to Maurice Colpron, Carolyn Relf and Sarah Sternbergh for facilitating our visit. Lucinda Leonard provided a constructive critical review of this manuscript. This is NRCan contribution number 20210433.

References

Baker, M.G., Heath, D.C., Schutt, D.L., Aster, R.C., Cubley, J.F. and Freymueller, J.T., 2019. The Mackenzie Mountains EarthScope Project: Studying Active Deformation in the Northern North American Cordillera from Margin to Craton. Seismological Research Letters, vol. 91, p. 521–532, doi:10.1785/0220190139.

Balfour, N.J., Cassidy, J.F., Dosso, S.E. and Mazzotti, S., 2011. Mapping crustal stress and strain in southwest British Columbia. Journal of Geophysical Research, vol. 116, p. 1–11, doi:10.1029/2010JB008003.

Bender, A. and Haeussler, P., 2017. Eastern Denali Fault Surface Trace Map, Eastern Alaska and Yukon, Canada. U.S. Geological Survey, Open-File Report 2017–1049, 10 p., https://doi.org/10.3133/of20171049.

Blackwell, D.D. and Richards, M., 2004. Geothermal Map of North America. American Association of Petroleum Geologists Map, https://www.smu.edu/Dedman/Academics/Departments/EarthSciences/Research/GeothermalLab/DataMaps/GeothermalMapofNorthAmerica, [accessed July 2019].

Blais-Stevens, A., Clague, J.J., Brahney, J., Lipovsky, P., Haeussler, P.J. and Menounos, B., 2020. Evidence for Large Holocene Earthquakes along the Denali Fault in Southwest Yukon, Canada. Environmental and Engineering Geoscience, vol. 26, p. 149–166, doi:10.2113/EEG-2263.

Bostock, H.S., 1952. Geology of the northwest Shakwak Valley, Yukon Territory. Geological Survey of Canada, Memoir 267, 50 p.

Busby, R.W. and Aderhold, K., 2020. The Alaska Transportable Array: As Built. Seismological Research Letters, v0l. 91, p. 3017–3027, doi:10.1785/0220200154.

Caine, J.S., Evans, J.P. and Forster, C.B., 1996. Fault zone architecture and permeability structure. Geology, vol. 24, p. 1025–1028, doi:10.1130/0091-7613(1996)024<1025.

Choi, M., Eaton, D.W. and Enkelmann, E., 2021. Is the Eastern Denali fault still active? Geology, vol. 49, doi:10.1130/G48461.1.

Clague, J.J., 1979. The Denali Fault System in southwest Yukon Territory -a geologic hazard? Geological Survey of Canada, Paper No. 79-1A, p. 169–178, doi:10.4095/104844.

Craig, J.W., 2018. Discovery and Analysis of a Blind Geothermal System in Southeastern Gabbs Valley, Western Nevada. Unpublished MSc thesis, University of Nevada, Reno, 121 p.

Curewitz, D. and Karson, J.A., 1997. Structural settings of hydrothermal outflow: Fracture permeability maintained by fault propagation and interaction. Journal of Volcanology and Geothermal Research, vol. 79, p. 149–168, doi:10.1016/S0377-0273(97)00027-9.

Dobson, P.F., 2016. A Review of Exploration Methods for Discovering Hidden Geothermal Systems. GRC Transactions, vol. 40, p. 695–706.

Eberhart-Phillips, D. *et al.*, 2003. The 2002 Denali Fault Earthquake, Alaska: A Large Magnitude, Slip-Partitioned Event. Science, vol. 300, p. 1113–1118, doi:10.1126/science.1082703.

Faulds, J. and Hinz, N., 2015. Favorable Tectonic and Structural Settings of Geothermal Systems in the Great Basin Region, Western USA: Proxies for Discovering Blind Geothermal Systems. Proceedings World Geothermal Congress 2015, Melbourne, Australia, p. 19–25.

Faulds, J.E., Hinz, N., Kreemer, C. and Coolbaugh, M., 2012. Regional Patterns of Geothermal Activity in the Great Basin Region, Western USA: Correlation With Strain Rates. GRC Transactions, vol. 36, p. 6.

Haeussler, P.J., Matmon, A., Schwartz, D.P. and Seitz, G.G., 2017. Neotectonics of interior Alaska and the late Quaternary slip rate along the Denali fault system. Geosphere, vol. 13, p. 1445–1463, doi:10.1130/GES01447.1.

IPCC, 2014. AR5 Climate Change 2014: Mitigation of Climate Change. Contribution of Working Group III to the Fifth Assessment Report of the Intergovernmental Panel on Climate Change, Cambridge University Press, 1967 p.

Jolie, E., Moeck, I. and Faulds, J.E., 2015. Quantitative structural-geological exploration of fault-controlled geothermal systems-A case study from the Basin-and-Range Province, Nevada (USA). Geothermics, vol. 54, p. 54–67, doi:10.1016/j.geothermics.2014.10.003.

Kristmannsdóttir, H. and Ármannsson, H., 2003. Environmental aspects of geothermal energy utilization. Geothermics, vol. 32, p. 451–461, doi:10.1016/S0375-6505(03)00052-X.

Leonard, L.J., Mazzotti, S. and Hyndman, R.D., 2008. Deformation rates estimated from earthquakes in the northern Cordillera of Canada and eastern Alaska. Journal of Geophysical Research: Solid Earth, vol. 113, p. 1–18, doi:10.1029/2007JB005456.

Lipovsky, P.S., Seitz, G., Haeussler, P.J., Crone, A.J., Schwartz, D.P., Clague, J.J., Mazotti, S. and Cobbett, R., 2009. Neotectonic investigations in southwest Yukon. In: Canadian Quaternary Association Meeting, Vancouver, BC, Canada.

Little, T.A., Morris, P., Hill, M.P., Kearse, J., Van Dissen, R.J., Manousakis, J., Zekkos, D. and Howell, A., 2021. Coseismic deformation of the ground during large-slip strike-slip ruptures: Finite evolution of “mole tracks”. Geosphere, vol. 17, p. 1170–1192, doi:10.1130/GES02336.1.

Majorowicz, J. and Grasby, S.E., 2010. Heat flow, depth–temperature variations and stored thermal energy for enhanced geothermal systems in Canada. Journal of Geophysics and Engineering, vol. 7, p. 232–241, doi:10.1088/1742-2132/7/3/002.

Marechal, A., Mazzotti, S., Elliott, J.L., Freymueller, J.T. and Schmidt, M., 2015. Indentor-corner tectonics in the Yakutat-St. Elias collision constrained by GPS. Journal of Geophysical Research: Solid Earth, vol. 120, p. 3897–3908, doi:10.1002/2014JB011842.

Marechal, A., Ritz, J.-F., Ferry, M., Mazzotti, S., Blard, P.-H., Braucher, R. and Saint-Carlier, D., 2018. Active tectonics around the Yakutat indentor: New geomorphological constraints on the eastern Denali, Totschunda and Duke River Faults. Earth and Planetary Science Letters, vol. 482, p. 71–80, doi:10.1016/j.epsl.2017.10.051.

McDermott, R.G., Ault, A.K. and Caine, J.S., 2021. Dating fault damage along the eastern Denali fault zone with hematite (U-Th)/He thermochronometry. Earth and Planetary Science Letters, vol. 563, doi:10.1016/j.epsl.2021.116872.

Meixner, J., Grimmer, J.C., Becker, A., Schill, E. and Kohl, T., 2018. Comparison of different digital elevation models and satellite imagery for lineament analysis: Implications for identification and spatial arrangement of fault zones in crystalline basement rocks of the southern Black Forest (Germany). Journal of Structural Geology, vol. 108, p. 256–268, doi:10.1016/j.jsg.2017.11.006.

Meixner, J., Schill, E., Grimmer, J.C., Gaucher, E., Kohl, T. and Klingler, P., 2016. Structural control of geothermal reservoirs in extensional tectonic settings: An example from the Upper Rhine Graben. Journal of Structural Geology, vol. 82, p. 1–15, doi:10.1016/j.jsg.2015.11.003.

Mira Geoscience, 2015. Ross River geothermal exploration project: Review of the 2014 work program. Yukon Geological Survey, Miscellaneous Report MR-18, 141 p.

Moeck, I.S., 2014. Catalog of geothermal play types based on geologic controls. Renewable and Sustainable Energy Reviews, vol. 37, p. 867–882, doi:10.1016/j.rser.2014.05.032.

Moeck, I., Kwiatek, G. and Zimmermann, G., 2009. Slip tendency analysis, fault reactivation potential and induced seismicity in a deep geothermal reservoir. Journal of Structural Geology, vol. 31, p. 1174–1182, doi:10.1016/j.jsg.2009.06.012.

Porter, C. *et al.*, 2018. ArcticDEM:, doi:10.7910/DVN/OHHUKH.

Ristau, J., Rogers, G.C. and Cassidy, J.F., 2007. Stress in western Canada from regional moment tensor analysis. Canadian Journal of Earth Sciences, vol. 44, p. 127–148, doi:10.1139/e06-057.

Seitz, G., Haeussler, P.J., Crone, A.J., Lipovsky, P.S. and Schwartz, D.P., 2008. Eastern Denali fault slip rate and paleoseismic history, Kluane Lake area, Yukon Territory, Canada. In: American Geophysical Union Fall Meeting, Abstract T53B-1947. AGU meeting, December 15–19, 2008, San Francisco, CA, USA.

Sibson, H., 1996. Structural permeability of fluid-driven fault-fracture meshes. Journal of Structural Geology, vol. 18, p. 1–12, doi:10.1016/0191-8141(96)00032-6.

Spotila, J.A. and Berger, A.L., 2010. Exhumation at orogenic indentor corners under long-term glacial conditions: Example of the St. Elias orogen, Southern Alaska. Tectonophysics, vol. 490, p. 241–256, doi:10.1016/j.tecto.2010.05.015.

Stewart, N., Gaudemer, Y., Manighetti, I., Serreau, L., Vincendeau, A., Dominguez, S., Mattéo, L. and Malavieille, J., 2018. "3D_Fault_Offsets," a Matlab Code to Automatically Measure Lateral and Vertical Fault Offsets in Topographic Data: Application to San Andreas, Owens Valley, and Hope Faults. Journal of Geophysical Research: Solid Earth, vol. 123, p. 815–835, https://doi.org/10.1002/2017JB014863.

Witter, J.B., 2020. Early-stage exploration for geothermal energy resources along the Denali fault near Duke River, Yukon. Yukon Geological Survey, Open File 2020-3, 70 p.

Zielke, O. and Arrowsmith, J.R., 2012. LaDiCaoz and LiDARimager—MATLAB GUIs for LiDAR data handling and lateral displacement measurement. Geosphere, vol. 8, p. 206–221, doi:10.1130/GES00686.1.

Zielke, O., Arrowsmith, J.R., Ludwig, L.G. and Akçiz, S.O., 2010. Slip in the 1857 and Earlier Large Earthquakes Along the Carrizo Plain, San Andreas Fault. Science, vol. 327, p. 1119–1122, doi:10.1126/science.1182781.